Numerical Simulations of Triaxial Test with Sand Using DEM

Łukasz Widuliński, Jan Kozicki, Jacek Tejchman

Faculty of Civil and Environmental Engineering, Gdańsk University of Technology,
ul. Narutowicza 11/12, 80-233 Gdańsk, Poland,
e-mails: lwidul@pg.gda.pl, jkozicki@pg.gda.pl, tejchmk@pg.gda.pl

Abstract

Numerical simulations of the behaviour of cohesionless sand were carried out using a discrete element method. A drained triaxial test of a homogeneous sand specimen under constant lateral pressure was modelled. To simulate the behaviour of sand, a 3D spherical discrete model YADE was used, enhanced by including rolling resistance in order to take into account grain roughness. Numerical results were directly compared with corresponding laboratory tests. The effects of lateral pressure, initial void ratio and micro-parameters on the global behaviour of sand were investigated.

Key words: discrete element model, rolling resistance, sand, triaxial test

List of Symbols

a_i –   acceleration of sphere i,

$\dot{A}$, $\dot{B}$ –   current orientation of sphere A and sphere B (unit quaternion related to global coordinate system),

$\dot{A}'$, $\dot{B}'$ –   orientation of sphere A and sphere B at contact,

$\vec{C}$ –   position of contact between two spheres,

E_c –   modulus of elasticity,

$\vec{F}_i$ –   force acting on sphere i,

$\vec{F}_n$ –   normal contact force,

$\vec{F}_s$ –   tangential contact force,

I_i –   moment of inertia of sphere i,

K_n –   normal stiffness of contact between two spheres,

K_r –   rotational stiffness of contact between two spheres,

K_s –   tangential stiffness of contact between two spheres,

m_i –   mass of sphere i,

$\vec{M}$ –   contact moment,

$\vec{M}_i$	–	moment acting on sphere i,
$\vec{N}$	–	normal vector of contact (vector of unit length),
$R_A,\ R_B$	–	radius of sphere A and sphere B,
U	–	penetration depth between two spheres,
$\vec{V}_A,\ \vec{V}_B$	–	current velocity of sphere A and sphere B,
$\vec{X}_A,\ \vec{X}_B$	–	current position of sphere A and sphere B,
α	–	damping coefficient,
β	–	dimensionless rotational stiffness coefficient,
Δt	–	time increment between two iterations,
$\Delta \dot{Q}$	–	orientation displacement increment between two spheres (unit quaternion),
$\Delta \vec{X}$	–	distance between centers of two spheres,
$\Delta \vec{V}$	–	velocity increment between two spheres,
$\Delta \vec{V}_S$	–	tangential velocity increment between two spheres,
$\Delta \vec{X}_S$	–	tangential displacement increment between two spheres,
$\Delta \vec{\omega}$	–	angular rotation increment between two spheres,
η	–	dimensionless rolling limit coefficient,
μ	–	inter-particle friction angle for spheres,
ν_c	–	Poisson's ratio of grain contact,
$\vec{\omega}_A,\ \vec{\omega}_B$	–	current rotation of sphere A and sphere B,
$\dot{\vec{\omega}}_A,\ \dot{\vec{\omega}}_B$	–	current angular velocity of sphere A and sphere B,
$\ddot{\vec{\omega}}_i$	–	rotational acceleration of sphere i.

1. Introduction

Granular materials consist of grains in contact and surrounding voids, which change their arrangement depending on environmental factors and initial density. Their micromechanical and fabric behaviour is inherently discontinuous, heterogeneous and non-linear. To describe their behavior, two main approaches are employed: continuum and discrete. In the former approach, simulations are performed at the global scale using the finite element method on the basis of e.g. elasto-plastic and hypoplastic constitutive models, enhanced by a characteristic length of micro-structure to describe strain localization (e.g. Tejchman and Wu 1993, Brinkgreve 1994, Tejchman 2004, Gudehus and Nübel 2004). In turn, the latter type involves simulations at the grain scale, i.e. each grain is modelled individually (Thornton et al 1996, Bardet 1998, Iwashita and Oda 1998, Peña et al 2007, Luding 2008). Such approaches are becoming increasingly popular for modelling granular materials due to ever faster processing speeds of computers and a possibility of connection to the FEM (Rojek 2007).

The aim of our calculations is to check the capability of a discrete element method to simulate the behavior of real cohesionless sand under monotonic load-

ing during a typical drained homogeneous triaxial test, which is among the most important geotechnical tests to determine soil properties. We have used the program YADE based on the so-called soft-particle approach developed at Grenoble University (Kozicki and Donze 2008, 2009, Belheine et al 2009). The effect of micro-parameters on the global behaviour of sand was studied carefully. To simulate the behaviour of real sand, a 3D spherical discrete model was used with rolling resistance in order to take into account grain roughness. The numerical results were quantitatively compared with the experimental data from triaxial tests performed by Wu (1992) at Karlsruhe University for so-called Karlsruhe sand.

The second author took part in the program development by implementing contact moments into a 3D YADE model.

2. Discrete Element Method

The discrete element method (DEM) is widely used to model a range of processes across many industries (Thornton et al 1996, Herrmann and Luding 1998, Jiang et al 2005, Kruyt and Rothenburg 2006, Zhu et al 2007, Ketterhagen et al 2008, Alonso-Marroquin et al 2008). The DEM is a numerical approach where statistical measures of the macro-mechanical response of material behavior are computed from the individual motion and mutual interactions of a large number of discrete elements (Cundall and Strack, 1979). It assumes, namely, that a solid material can be represented by a collection of particles interacting among themselves in the normal and tangential direction. The state of every particle in the system and all particle interactions are determined using physical laws. This method provides new insight into constitutive modeling, because a physical process which governs the constitutive behavior can be described at the local scale which is usually responsible for the global behaviour. This approach is particularly advantageous due to the high level of detail in the output describing the behavior of the particles. In spite of their simplicity, particle-based models are able to reproduce the complex structure of the incremental stress-strain response of granular materials (Calvetti et al 2003). The limitations of the method are: necessity of long computational time and difficulty of experimental validation.

In our model, the so-called soft-particle approach is used (i.e. the model allows for particle deformation which is modeled as an overlap of particles). The dynamic behaviour of the discrete system is solved numerically using a force-displacement Lagrangian approach and tracks the positions, velocities, and accelerations of each particle individually. It uses an explicit finite difference algorithm, assuming that velocities and accelerations are constant in each time step. To calculate forces acting in particle-particle or particle-wall contacts, a particle interaction model is assumed in which the forces are typically decomposed into normal and tangential components. The total forces and moments acting on each particle are summed. Next, the problem is reduced to the integration of Newton's equations of motion

for both translational and rotational degrees of freedom. As a result, the accelerations of each particle are obtained. The time step is incremented and accelerations are integrated over time to determine updated particle velocities and positions. To maintain the numerical stability of the method and to obtain a quick convergence to a quasi-static state of equilibrium of the assembly of particles, damping forces have to be introduced.

Discrete elements can have different geometries (Ketterhagen et al 2008), but to keep a low calculation cost, usually the simplest spherical geometry is chosen (dealing with realistic shapes would lead to a prohibitive calculation cost). However, such a spherical geometry is too idealized to accurately model phenomena exhibited by real granular materials. It has been shown that spherical particles have a smaller angle of repose and reduced shear strength as compared to non-spherical particles (Rothenburg and Bathurst 1992, Poeschel and Buchholz 1993). This is due to the fact that the rotation is only resisted by frictional contacts with neighbouring particles; whereas for non-spherical particles, the rotation tends to be inhibited by mechanical interlocking.

In the paper, only spherical elements were used. To simulate grain roughness, moments were introduced into a 3D model which were transferred through contacts and which resisted particle rotations (Kozicki and Donze 2008, 2009). In this way, grains are in contact with their neighbours through a certain contact surface. The importance of rolling resistance on the contact behaviour of granular bodies in 2D simulations was shown, among others, by Oda et al (1997), Iwashita and Oda (1998) and Jiang et al 2005.

A complete set of formulae used in this model is presented in Table 2 in Appendix A. Below, only the most important ones are listed. A complete set of symbols used is listed in the List of Symbols of the beginning of the paper.

Figure 1 presents two spherical discrete elements A and B in contact. The radii of two spheres are R_A and R_B. The positions of their centres are denoted by X_A and X_B. During each time step, two spheres may remain in contact. The interaction force vector $\vec{F}$ represents the action of the element A on the element B and may be decomposed into a normal $\vec{F}_n$ and tangential vector $\vec{F}_s$, respectively. Both forces are linked to displacements through the normal stiffness K_n and tangential stiffness K_s

$$\vec{F}_n = K_n U \vec{N}, \tag{1}$$

$$\vec{F}_s = \vec{F}_s + K_s \Delta \vec{X}_s, \tag{2}$$

where U is the penetration depth between elements, $\vec{N}$ denotes the normal vector at the contact point and $\Delta \vec{X}_s$ is the incremental tangential displacement. The tangential force $\vec{F}_s$ is obtained by summing its increments. The stiffness parameters
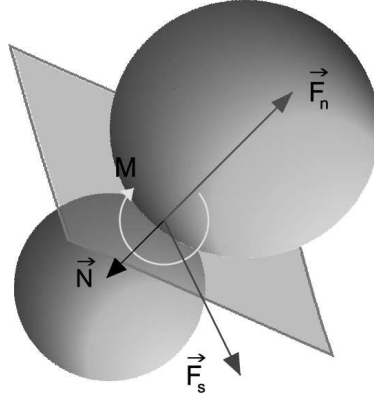
Fig. 1. Two spheres in contact ($\vec{F}_s$ – tangential contact force vector, $\vec{F}_n$ – normal contact force vector, $\vec{M}$ – contact moment vector, $\vec{N}$ – contact normal vector)

are calculated with the aid of the modulus of elasticity of the grain contact E_c and grain radii R (to determine the normal stiffness K_n) or with the aid of the modulus of elasticity E_c and Poisson's ratio ν_c of the grain contact, and grain radii R (to determine the tangential stiffness K_s) of two neighbouring spheres, respectively:

$$K_n = E_c \frac{2R_A R_B}{R_A + R_B} \quad \text{and} \quad K_s = E_c \nu_c \frac{2R_A R_B}{R_A + R_B}. \tag{3}$$

If $R_A = R_B = R$, the stiffness parameters are equal to: $K_n = E_c R$ and $K_t = \nu_c E_c R$ (thus $K_n/K_s = 1/\nu_c$), respectively. Shearing starts at the contact point when the contact forces $\vec{F}_s$ and $\vec{F}_n$ satisfy a frictional Mohr-Coulomb equation (Fig. 2)

$$\left\| \vec{F}_s \right\| - \left\| \vec{F}_n \right\| \tan\mu \leq 0 \tag{4}$$

with μ denoting the inter-particle friction angle.

The program YADE differs from other DEM codes by the fact that contact moments between spheres are introduced to increase the rolling resistance. Consequently, the real grain roughness can be simulated in 3D simulations. Only the normal force contributes to rolling resistance. The contact moment increments are calculated using the rolling stiffness K_r

$$\Delta M = K_r \Delta \vec{\omega}, \tag{5}$$
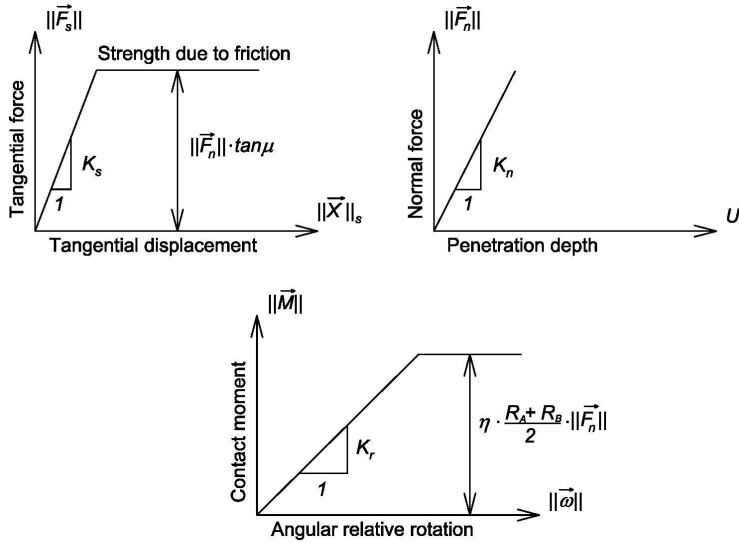
with

$$K_r = \beta K_s R_A R_B, \tag{6}$$

Fig. 2. Mechanical response of normal, tangential and rolling contact model (Kozicki et al 2008)
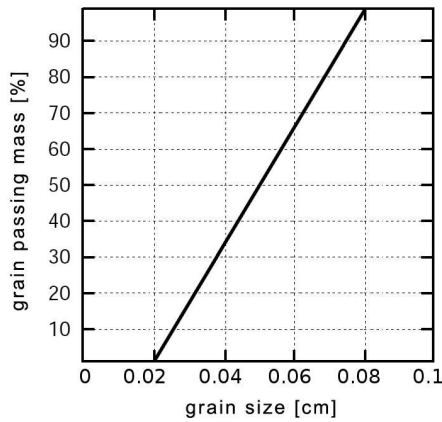

Fig. 3. Grain distribution curve for sand assumed for numerical simulations of a monotonic triaxial test (mean grain diameter $d_{50} = 0.5$ mm)

where $\Delta\vec{\omega}$ is the angular increment rotation between two spheres (see the List of Symbols) and β is the dimensionless rolling stiffness coefficient. In turn, the dimensionless coefficient η controls the limit of the rolling behavior (Fig. 2)

$$\left\|\vec{M}\right\| - \eta \frac{R_A + R_B}{2}\left\|\vec{F_n}\right\| \le 0. \tag{7}$$

No forces and moment are transmitted when grains are separated. Figure 2 displays the assumed normal, tangential and rolling contact relationships in the model. To dissipate kinetic energy, a local non-viscous damping scheme was adopted (Cundall and Hart 1992):

$$\vec{F}^k = \vec{F}^k - \alpha \cdot \text{sgn}(\vec{V}^k)\left|\vec{F}^k\right|, \tag{8}$$

$$\vec{M}^k = \vec{M}^k - \alpha \cdot \text{sgn}(\vec{\omega}^k)\left|\vec{M}^k\right|. \tag{9}$$

A positive numerical damping coefficient α is smaller than 1 ($\text{sgn}(\cdot)$ returns the sign of the argument). The equations are separately applied to each k-th component of a 3D vector. In general, the damping parameter α can be different for each translational and rotational degree of freedom (but this is not the case in our calculations).

As compared to other discrete models incorporating contact moments (e.g. to the 2D model by Jiang et al 2005), the program YADE is designed primarily for 3D simulations, rolling resistance is an independent parameter, rotations are described by means of quaternions, and a grain shape coefficient is not included.

The following five main local material parameters are needed for discrete simulations: E_c, v_c, β, μ and η, which were calibrated with corresponding triaxial laboratory test results with Karlsruhe sand (Wu 1992). In addition, the particle radius R, particle density ρ and damping parameters α are required.

3. Triaxial Test

The numerical results of a triaxial test for cohesionless sand were directly compared with the corresponding experimental results of several triaxial tests performed by Wu (1992) at Karlsruhe University with so-called Karlsruhe sand (Figs. 5 and 6). In numerical comparative simulations of a homogeneous triaxial test, a cubic granular specimen of $10 \times 10 \times 10$ cm^3 including about 10000 spheres with a radius varying between 0.2 mm and 0.8 mm ($d_{50} = 0.5$ mm) was used (Fig. 3). The spheres were distributed at random. The test was modeled using confining smooth rigid wall elements (Fig. 4). Isotropic compression took place under gravity free conditions. The top and bottom boundaries moved vertically as loading platens under strain-controlled conditions to simulate the confining pressure p. The initial density of a granulate was obtained using a radius expansion method based on
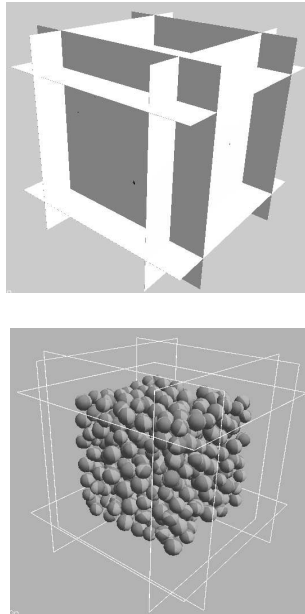
Fig. 4. Simulation of a monotonic triaxial test for sand using DEM

a Weibull distribution (Kozicki and Donze 2008). In this method, the inter-particle friction was assumed to be zero and gravity was varied to obtain a different initial density caused by grain overlapping (thus, it was possible to exactly reproduce the experimental value). The initial void ratio e_o was varied between $e_o = 0.50$ for an initially dense specimen and $e_o = 0.90$ for an initially loose specimen.

Table 1 lists the material parameters assumed in discrete simulations. The numerical damping was $\alpha = 0.3$ for each translational and rotational degree of freedom (its effect on our quasi-static results was negligible). In turn, the particle density was $\rho = 2.6$ kNs^2/m.

4. Numerical Results

Figure 7 shows a direct comparison between numerical and experimental results (Wu 1992) with initially very dense Karlsruhe sand ($e_o = 0.53$, $d_{50} = 0.5$ mm) at confining pressure $p = 200$ kPa up to $\varepsilon_1 = 12\%$. Both experimental curves (global axial normal stress versus global axial strain and global volumetric strain versus global axial strain) are reproduced very well. The calculated maximum internal friction angle, $\phi = 42.3°$, compares well with the experimental value of $\phi = 43.7°$ (Wu 1992) (Fig. 6). The calculated dilatancy angle $\psi = 27.1°$ and modulus of elasticity $E = 101$ MPa are also in a satisfactory agreement with experimental results of $\psi = 28.5°$ and $E = 104$ MPa (Fig. 6).

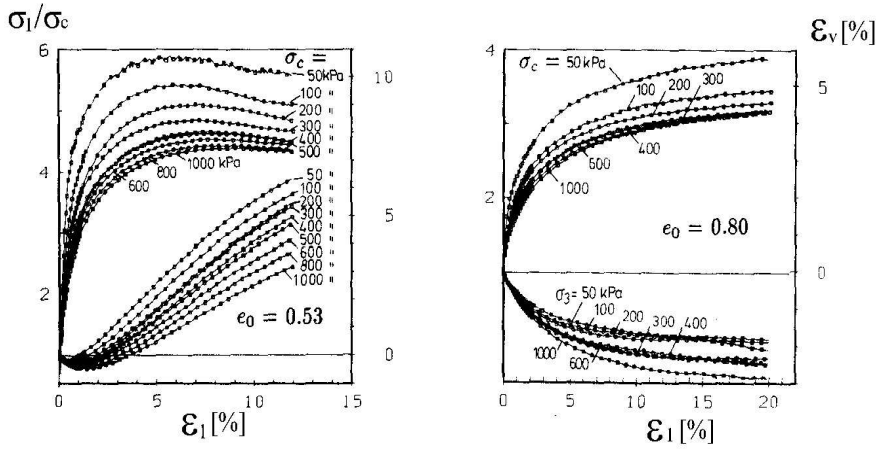**Fig. 5.** Experimental results of triaxial tests by Wu (1992): relationship between σ_1/σ_c and ε_1, and between ε_v and ε_1 for Karlsruhe sand at different confining pressures σ_c: A) initially very dense ($e_o = 0.53$) sand, B) initially loose sand ($e_o = 0.80$) (σ_1 – vertical axial stress, ε_1 – vertical axial strain, ε_v – volumetric strain)

Table 1. Microscopic material parameters for discrete simulations

Material parameters	Value
Modulus of elasticity of grain contact E_c [GPa]	3–30
Poisson's ratio of grain contact ν_c [–]	0.3
Grain size [mm]	0.2 – 0.8 mm or 2.0 – 8.0 mm
Mean grain diameter d_{50} [mm]	0.5 mm or 5.0 mm
Normal stiffness K_n [kPa]	7.5×10^3 ($d_{50} = 0.5$ mm)
	7.5×10^4 ($d_{50} = 5.0$ mm)
Tangential stiffness K_s [kPa]	2.25×10^3 ($d_{50} = 0.5$ mm)
	2.25×10^4 ($d_{50} = 5.0$ mm)
Inter-particle friction angle μ [°]	20 – 40
Rolling stiffness coefficient β [–]	0.1 – 50.0
Moment limit coefficient η [–]	0.1 – 3.0
Initial void ratio e_0 [–]	0.53 – 0.90
Mass density ρ [kNs^2/m]	2.6
Damping coefficient α [–]	0.3

The initial simulations showed a small effect of the mean grain diameter on the results of the global internal friction angle at peak (which was smaller by 5% only with $d_{50} = 0.5$ mm, Fig. 8). The shape of both curves with a different d_{50} was similar due to the fact that shear localization was not taken into account. Therefore, to save computation time, subsequent discrete simulations, showing the capabilities of DEM, were carried out with $d_{50} = 5$ mm using the same parameters as for $d_{50} = 0.5$ mm (2000 spheres were used).
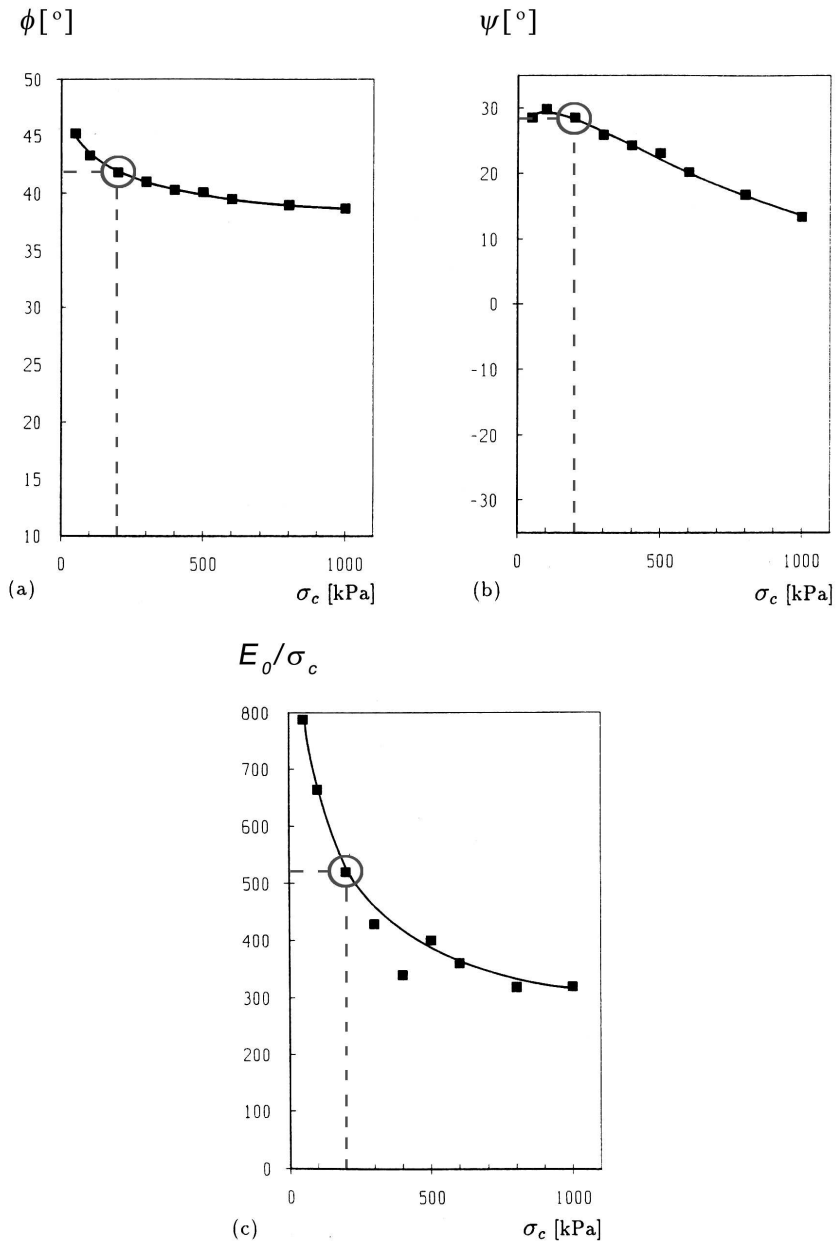
Fig. 6. Experimental results of triaxial tests for initially very dense sand ($e_o = 0.53$): (a) effect of confining pressure σ_c on maximum internal friction angle ϕ, (b) dilatancy angle ψ, (c) normalized modulus of elasticity E_0/σ_c (Wu 1992)
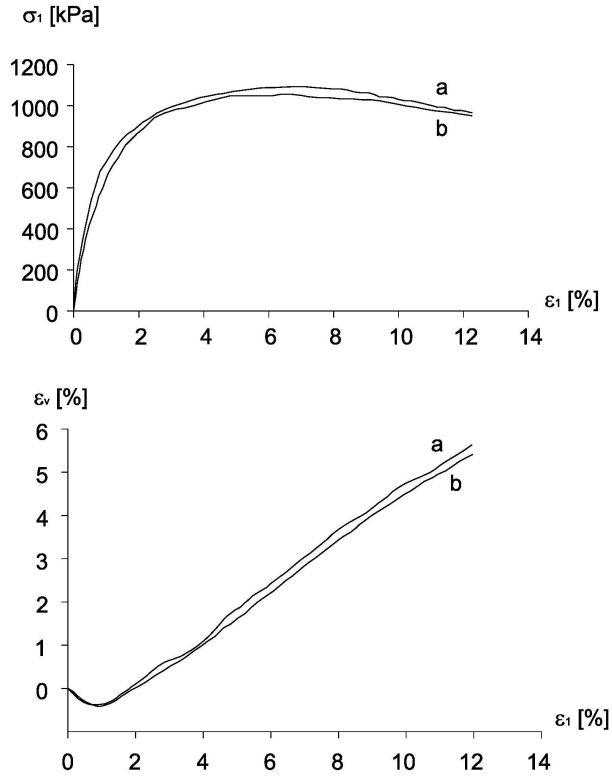
Fig. 7. Triaxial test for granular specimen: vertical stress versus vertical axial strain and volumetric strain versus axial strain (p = 200 kPa, e_0 = 0.53, d_{50} = 0.5 mm): a) experiment (Wu 1992), b) discrete simulation (E_c = 30 GPa, v_c = 0.3, μ = 30°, η = 1.0, β = 0.15)

4.1. Effect of the Contact Moments

Figure 9 demonstrates the influence of contact moments on the behaviour of initially dense sand (μ = 30°, η = 1.0, p = 100 kPa, e_0 = 0.60, d_{50} = 5 mm). The rolling stiffness coefficient was β = 0.15 (with contact moments) or β = 0 (no contact moments). The test was performed until a critical state was reached. The numerical results of the deviatoric stress versus axial strain and volumetric strain versus the axial strain show a huge impact of contact moments. In the case of contact moments (β = 0.15), a significant increase of the initial stiffness, global internal friction angle at peak ϕ^p and at the residual state ϕ_{res}, dilatancy angle ψ and material softening occurs. The elastic modulus is 95 MPa (with contact moments) or 32 MPa (without contact moments). The global peak internal friction angle ϕ^p (calculated with principal stresses from the Mohr's equation) grows from 22° up to 40°, global residual internal friction angle ϕ_{res} increases from 11° up to 29°, and the dilatancy angle ψ rises from 4° up to 16°, respectively. The results show that the rolling effect is very pronounced.
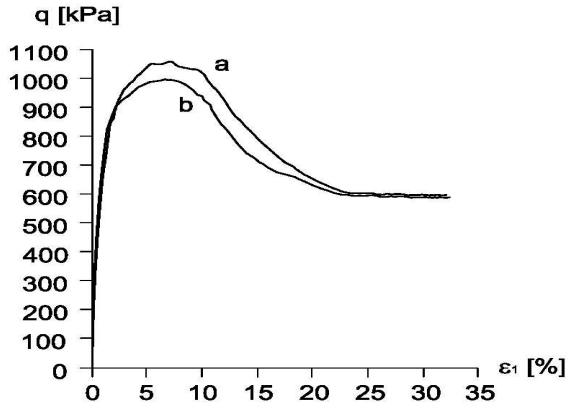
Fig. 8. Discrete simulations of triaxial test for granular specimen: global deviatoric stress versus axial strain (E_c = 30 GPa, v_c = 0.3, μ = 30°, β = 0.15, η = 1.0, p = 200 kPa, e_0 = 0.53): a) d_{50} = 5 mm, b) d_{50} = 0.5 mm
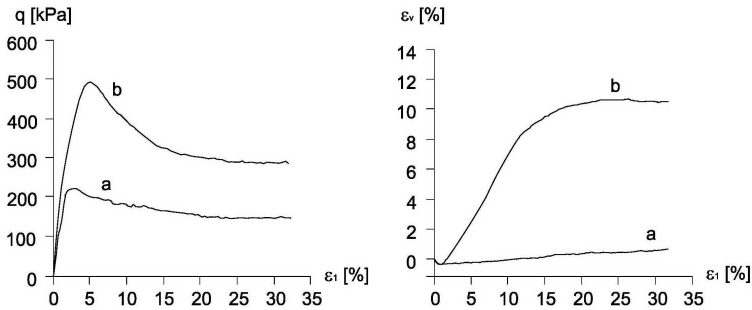

Fig. 9. Discrete simulations of triaxial test for granular specimen: global deviatoric stress and volumetric strain versus axial strain (E_c = 30 GPa, v_c = 0.3, μ = 30°, η = 1.0, p = 100 kPa, e_0 = 0.60, d_{50} = 5 mm): a) calculations without contact moments (β = 0), b) calculations with contact moments (β = 0.15)

4.2. Effect of Inter-Particle Internal Friction Angle

The numerical results (global deviatoric stress versus axial strain and global volumetric strain versus axial strain) with the inter-particle friction angle μ changing between 20° and 40° are shown in Figs. 10 and 11 for initially dense sand (η = 1.0, β = 0.15, p = 100 kPa, e_0 = 0.60, d_{50} = 5 mm). The local friction angle μ has a strong effect on both the peak stress and dilatancy angle, but an insignificant effect on the residual deviatoric stress. An increase of μ obviously causes the growth of ϕ^p and ψ. Dependent upon μ, the calculated maximum and residual overall internal friction angles ϕ are 35° − 45° and 30°, respectively (Fig. 11). The dilatancy angle ψ varies between 6° (μ = 20°) and 16° (μ = 40°).
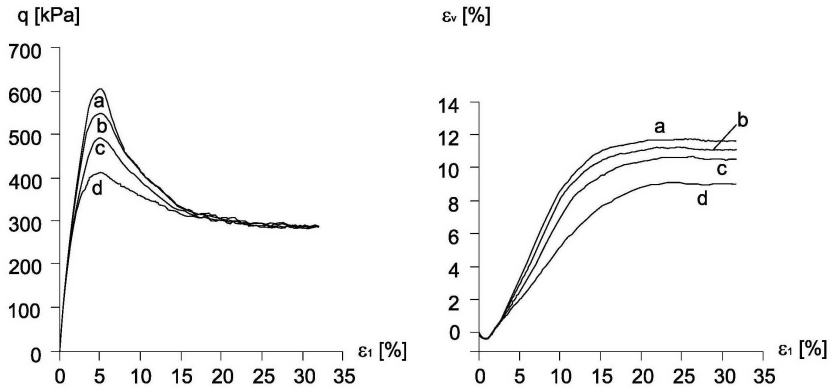
Fig. 10. Discrete simulations of triaxial test for granular specimen: global deviatoric stress and volumetric strain versus axial strain for different inter-particle local friction angle μ: a) 40°, b) 35°, c) 30°, d) 20° (E_c = 30.0 GPa, v_c = 0.3, μ = 30°, β = 0.15, η = 1.0, p = 100 kPa, e_0 = 0.60, d_{50} = 5 mm)
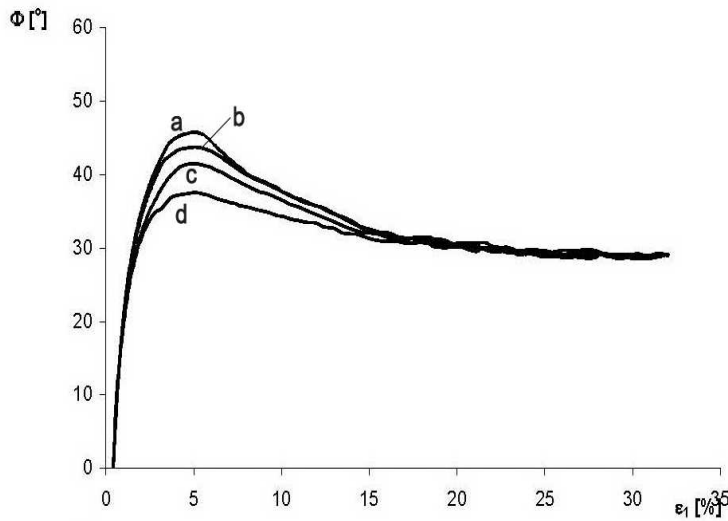

Fig. 11. Discrete simulations of triaxial test for granular specimen: global internal friction angle ϕ versus axial strain: a) μ = 40°, b) μ = 35°, c) μ = 30°, d) μ = 20° (E_c = 10.0 GPa, v_c = 0.3, μ = 30°, β = 0.15, η = 1.0, p = 100 kPa, e_0 = 0.60, d_{50} = 5 mm)

4.3. Effect of Rolling Stiffness

The effect of rolling stiffness coefficient β in the range of 0.10–50 is presented in Fig. 12 (p = 100 kPa, e_0 = 0.60, d_{50} = 0.5 cm). The coefficient has a very strong effect on the entire stress-strain curve and a small effect on volume changes. The higher the parameter β, the greater is the mobilized global internal friction angle.
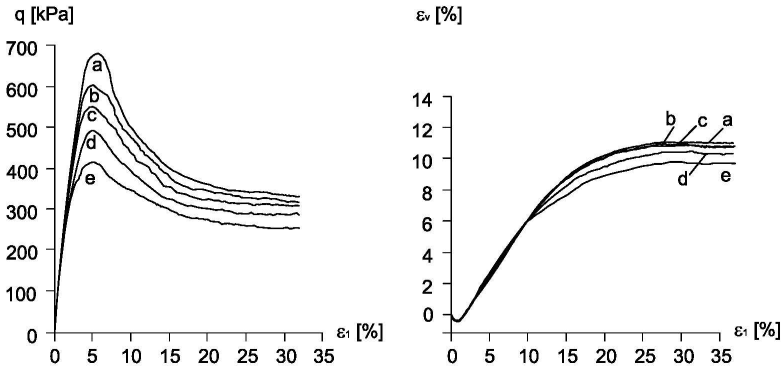
Fig. 12. Discrete simulations of triaxial test for granular specimen: global deviatoric stress and volumetric strain versus axial strain for different rolling stiffness parameter β: a) $\beta = 0.10$, b) $\beta = 0.15$, c) $\beta = 1.0$, d) $\beta = 3.0$, e) $\beta = 50$ ($E_c = 30$ GPa, $v_c = 0.3$, $\mu = 30°$, $\beta = 0.15$, $\eta = 1.0$, $p = 100$ kPa, $e_0 = 0.60$, $d_{50} = 5$ mm)

4.4. Effect of Moment Limit Coefficient

Figure 13 demonstrates the influence of the coefficient η varying between 0.1–3.0 ($p = 100$ kPa, $e_0 = 0.60$, $d_{50} = 5$ mm). The coefficient has a pronounced influence on the stress-strain curve up to the residual state but an insignificant effect on volume changes. The higher the coefficient η, the greater is the peak global friction angle.
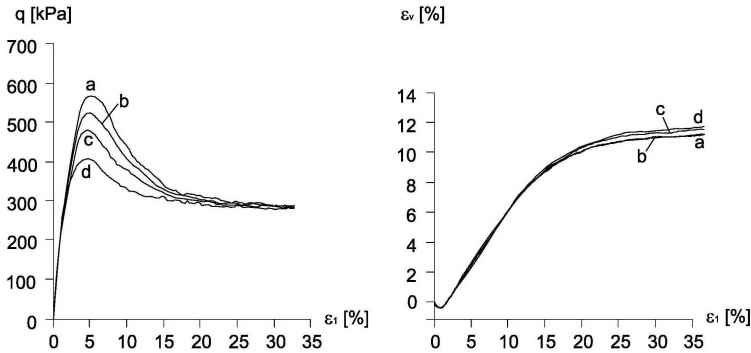

Fig. 13. Discrete simulations of triaxial test for granular specimen: global deviatoric stress and volumetric strain versus axial strain for different parameter η: a) $\eta = 3.0$, b) $\eta = 1.0$, c) $\eta = 0.15$, d) $\eta = 0.1$ ($E_c = 30.0$ GPa, $v_c = 0.3$, $\mu = 30°$, $\beta = 0.15$, $\eta = 1.0$, $p = 100$ kPa, $e_0 = 0.60$, $d_{50} = 5$ mm)

4.5. Effect of Modulus of Elasticity of Contact

The effect of the normal and tangential stiffness in initially dense specimen ($p = 100$ kPa, $e_0 = 0.60$, $d_{50} = 5$ mm) is presented in Fig. 14 (the contact modulus of elasticity
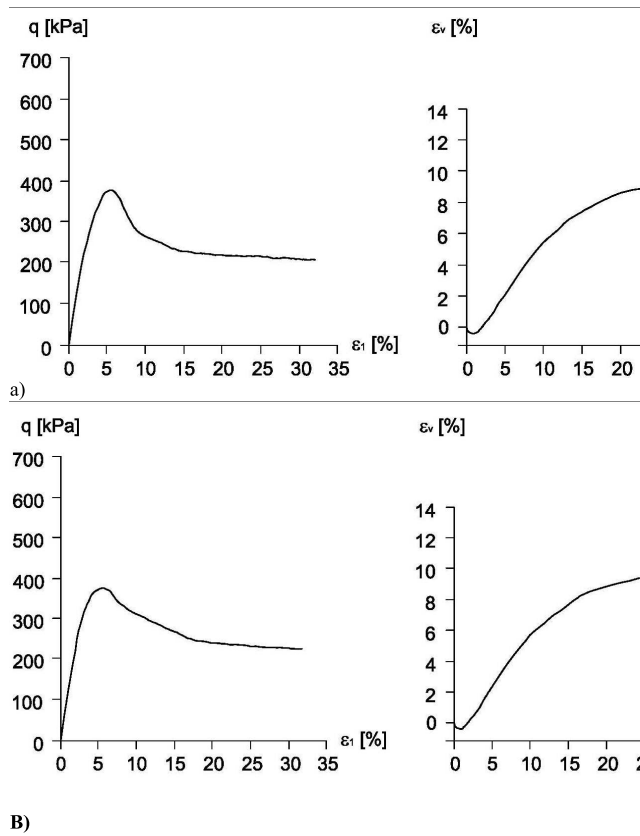
Fig. 14. Discrete simulations of triaxial test for granular specimen: global deviatoric stress and volumetric strain versus axial strain for different parameter E_c ($\mu = 30°$, $\eta = 1.0$, $\beta = 0.15$, $p = 100$ kPa, $e_0 = 0.60$, $d_{50} = 5$ mm): a) $E_c = 30$ GPa, b) $E_c = 3$ GPa

E_c was decreased by the factor 10). The global modulus of elasticity and Poisson's ratio of sand grow with increasing E_c: from $E = 82$ MPa and $\nu = 0.18$ (with $E_c = 3$ GPa) up to $E = 95$ MPa and $\nu = 0.26$ (with $E_c = 30$ GPa).

4.6. Effect of Confining Pressure

Figure 15 demonstrates the numerical results with an initially dense specimen ($e_0 = 0.60$, $d_{50} = 5$ mm) for a larger confining pressure of $p = 300$ kPa. Similarly as in the experiment (Fig. 5, Wu 1992), the global peak internal friction angle ϕ^p decreases with increasing p ($\phi^p = 40°$ for $p = 100$ kPa and $\phi^p = 39°$ for $p = 300$ kPa). The global residual internal friction angle ϕ_{res} decreases with p as well ($\phi_{res} = 30°$ for $p = 100$ kPa, $\phi_{res} = 29°$ for $p = 300$ kPa). In turn, the dilatancy angle ψ is reduced from $\psi = 16°$ at $p = 100$ kPa to $\psi = 14°$ at $p = 300$ kPa.
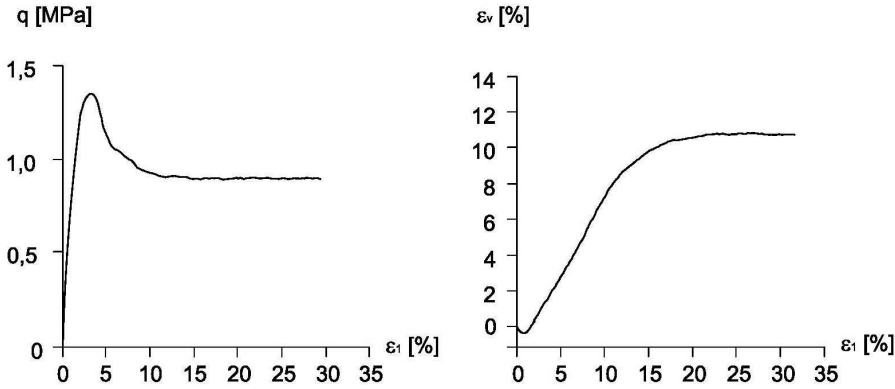
Fig. 15. Discrete simulations of triaxial test for granular specimen for $p = 300$ kPa: global deviatoric stress and volumetric strain versus axial strain ($E_c = 30$ GPa, $\nu_c = 0.3$, $\mu = 30°$, $\beta = 0.15$, $\eta = 1.0$, $e_0 = 0.60$, $d_{50} = 5$ mm)
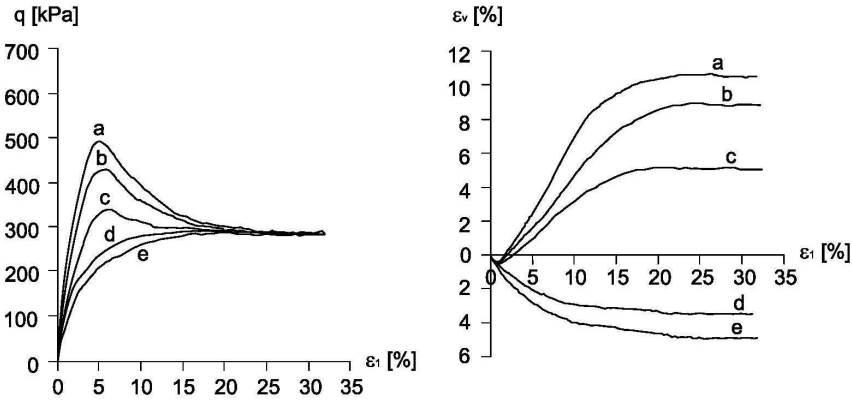

Fig. 16. Discrete simulations of triaxial test for granular specimen: global deviatoric stress and volumetric strain versus axial strain for different initial void ratio e_0: a) $e_0 = 0.50$, b) $e_0 = 0.60$, c) $e_0 = 0.70$, d) $e_0 = 0.80$, e) $e_0 = 0.90$ ($E_c = 30$ GPa, $\nu_c = 0.3$, $\mu = 30°$, $\beta = 0.15$, $\eta = 1.0$, $p = 100$ kPa, $d_{50} = 5$ mm)

4.7. Effect of Initial Void Ratio

The numerical results (deviatoric stress versus axial strain and volumetric strain versus axial strain) for different initial void ratios of sand ($e_0 = 0.50 \div 0.90$) are demonstrated in Fig. 16 ($p = 100$ kPa, $d_{50} = 0.5$ cm). Similarly as in the real experiment (Fig. 5, Wu 1992), initially loose granulates indicate continuous hardening (the peak strength is not observed) connected to contractancy only. The initially dense specimens exhibit a higher initial stiffness than the loose ones. The contractancy and dilatancy increase with increasing and decreasing e_0, respectively. All calculated curves reach, at large vertical strain of 20%, the same value of the stress deviator, with the granular specimen deforming at constant volume, i.e.
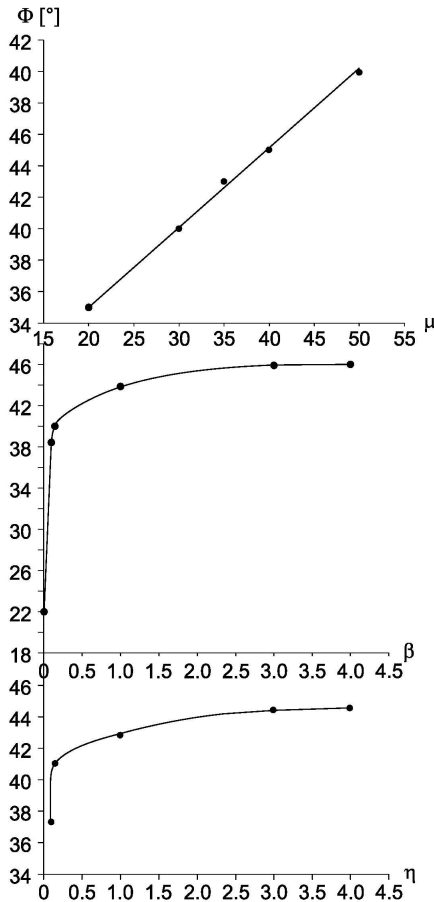
Fig. 17. Effect of local material parameters μ, β and η on global internal friction angle at peak during triaxial test from discrete simulations (E_c = 30 GPa, v_c = 0.3, μ = 30°, β = 0.15, η = 1.0, p = 100 kPa, e_0 = 0.60, d_{50} = 5 mm)

a critical state is always reached independently of initial void ratio. The global residual internal friction angle is almost identical and is equal to 28°.

4.8. Effect of Micromechanical Parameters

Figures 17–19 present the effect of the micromechanical parameters (inter-particle friction angle μ, rolling stiffness coefficient β and moment limit coefficient η) on the global predictions (internal friction angle at peak ϕ^p, internal friction angle at the residual state ϕ_{res} and dilatancy angle ψ) for σ_c = 100 kPa, e_0 = 0.60 and d_{50} = 0.5 cm.

The internal friction angle at peak, internal friction angle at the residual state, and dilatancy angle increase with increasing β and η (relationship is parabolic) and
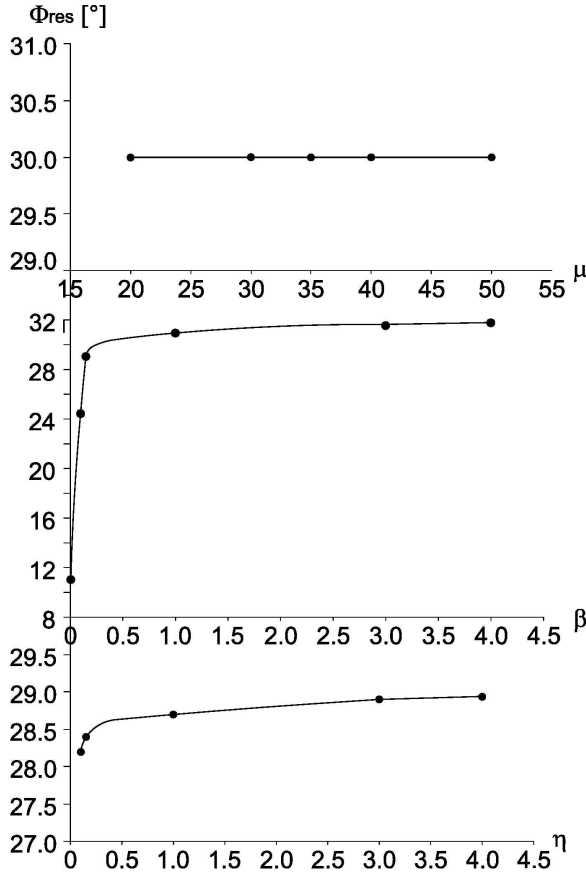
Fig. 18. Effect of local material parameters μ, β and η on global internal friction angle at residual state during triaxial test from discrete simulations ($E_c = 30$ GPa, $v_c = 0.3$, $\mu = 30°$, $\beta = 0.15$, $\eta = 1.0$, $p = 100$ kPa, $e_0 = 0.60$, $d_{50} = 5$ mm)

reach an asymptote at $\beta \approx 5$ and $\eta \approx 5$, respectively. In turn, the internal friction angle at peak increases linearly with μ. The internal friction angle at the residual state does not depend on μ and the dilatancy angle increases non-linearly with increasing μ reaching an asymptote at $\mu \approx 50°$.

4.9. Internal Work, External Work and Dissipation

Finally, Figs. 20 and 21 show the calculated internal work, external work and dissipation in initially dense sand of Fig. 7 ($E_c = 30$ GPa, $v_c = 0.3$, $\mu = 30°$, $\eta = 1.0$, $\beta = 0.15$, $p = 200$ kPa, $e_0 = 0.53$, $d_{50} = 0.5$ mm). The internal work δU was done by contact tangential forces on tangential displacements, contact normal forces on penetration depths and contact moments on angular rotations. The external work δW was done by the external vertical force and horizontal forces on vertical and
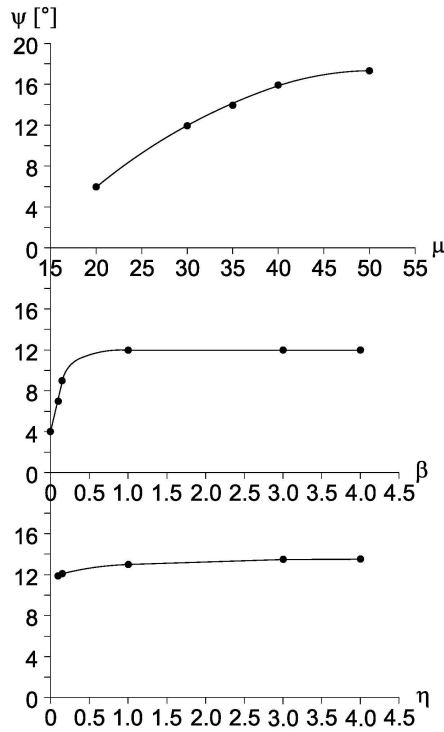
Fig. 19. Effect of local material parameters μ, β and η on global dilatancy angle during triaxial test from discrete simulations ($E_c = 30$ GPa, $\nu_c = 0.3$, $\mu = 30°$, $\beta = 0.15$, $\eta = 1.0$, $p = 100$ kPa, $e_0 = 0.60$, $d_{50} = 5$ mm)

horizontal displacements, respectively. The total dissipation δD was calculated from the difference between the external work done on the assembly and internal work done by contact forces and moments.

Fig. 20. Triaxial test for granular specimen: a) external work, b) internal work, c) dissipation from discrete simulations ($E_c = 30$ GPa, $\nu_c = 0.3$, $\mu = 30°$, $\eta = 1.0$, $\beta = 0.15$, $p = 200$ kPa, $e_0 = 0.53$, $d_{50} = 0.5$ mm)

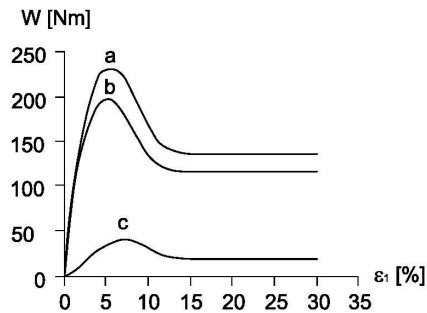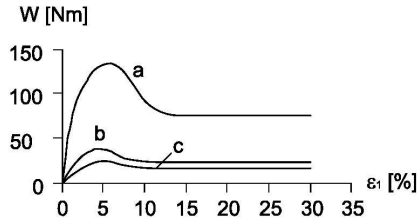**Fig. 21.** Internal work done by normal contact forces a), tangential contact forces b) and contact moments c) from discrete simulations (E_c = 30 GPa, ν_c = 0.3, μ = 30°, η = 1.0, β = 0.15, p = 200 kPa, e_0 = 0.53, d_{50} = 0.5 mm)

The evolutions of three components of the internal work (Fig. 21) are similar to the evolution of shear strength (Fig. 7). The largest internal work was performed by contact normal forces (50% at the residual state) and the smallest was by contact moments (20% at the residual state). The total dissipation was about 20% at peak and 10% at the residual state, respectively.

5. Conclusions

The numerical simulations of a triaxial test show that a simplified numerical model based on the discrete element method is capable of reproducing the most important macroscopic properties of cohesionless granular materials without necessitating a description of the granular structure perfectly. Comparing the numerical simulations with the experimental triaxial tests conducted with different initial void ratios and confining pressures shows that the model is able to predict realistically the experimental results for cohesionless sand.

The sand grain roughness can be modeled by means of spheres with contact moments. The presence of contact moments has a significant effect on the global behavior of sand (stress-strain curve and volumetric curve).

The model is capable of closely reproducing the behavior of cohesionless soils in the elastic, contraction, and dilatancy phase and at the critical state. At large strains, the granular specimen always reaches a critical state independently of its initial density.

The model requires five main micro-mechanical parameters: contact modulus of elasticity, contact Poisson's ratio, rolling contact stiffness parameter β, inter-particle friction angle μ and rolling limit parameter η, which can all be calibrated effectively with a true geotechnical triaxial test.

The peak global internal friction angle is controlled by micromechanical parameters μ, β and η. The residual internal friction angle is affected by β only. In turn, the dilatancy angle is solely affected by μ.

The higher the confining pressure, the smaller are both the global friction and dilatancy angle.

Our research will be continued. The discrete simulations will be carried out with sand by taking into account shear localization.

References

Alonso-Marroquin F., Mühlhaus H. B. and Herrmann H. (2008) Micromechanical investigation of granular ratcheting using a discrete model of polygonal particles, *Particulology,* 6, 390–403.

Bardet J. P. (1998) *Introduction to computational granular mechanics*, [in:] *Behaviour of Granular materials*, (ed. B. Cambou), CISM 385, Udine, Springer, 99–171.

Belheine N., Plassiard J. P., Donze F. V., Darve F. and Seridi A. (2009) Numerical simulations of drained triaxial test using 3D discrete element modeling, *Computers and Geotechnics*, 11 (5).

Brinkgreve R. (1994) Geomaterial models and numerical analysis of softening. *Dissertation*, Delft University, 1–153.

Calvetti F., Viggiani G. and Tamagnini C. (2003) Micromechanical inspection of constitutive modeling, *Proc. Int. Conf. Constitutive modelling and analysis of boundary value problems in geotechnical engineering*, Hevelius Edizioni, Benevento, 187–216.

Cundall P. A. and Strack O. D. L. (1979) The distinct numerical model for granular assemblies, *Geotechnique*, **29**, 47–65.

Cundall P. A. and Hart R. (1992) Numerical modeling of discontinua, *J. Eng. Comp.*, 9, 101–113.

Gudehus G. and Nübel K. (2004) Evolution of shear bands in sand, *Geotechnique*, **54** (3), 187–201.

Herrmann H. J. and Luding S. (1998) Modeling granular media on the computer, *Continuum Mech. Therm.*, **4** (10), 189–231.

Iwashita K. and Oda M. (1998) Rolling resistance at contacts in simulation of shear band development by DEM, *ASCE J. Eng. Mech.,* **124** (3), 285–292.

Jiang M. J., Yu H.-S. and Harris D. (2005) A novel discrete model for granular material incorporating rolling resistance, *Computers and Geotechnics*, **32**, 340–357.

Ketterhagen W. R., Amende M. T. and Hancock B. C. (2008) Process modeling in the pharmaceutical industry using the discrete element method, *Pharmaceutical Research and Development*, DOI 10.1002/jps.21466.

Kozicki J. and Donze F. V. (2008) A new open-source software developed for numerical simulations using discrete modelling methods, *Computer Methods in Applied Mechanics and Engineering*, **197**, 4429–4443.

Kozicki J. and Donze F. V. (2009) Yade-open DEM: an open-source software using a discrete element method to simulate granular material, *Engineering Computations*, **26** (7–8), 786–805.

Kruyt N. P. and Rothenburg L. (2006) Shear strength, dilatancy, energy and dissipation in quasi-static deformation of granular materials, JSTAT/2006/P07021.

Luding S. (2008) Cohesive, frictional powders: contact models for tension, *Granular Matter*, **10** (4), 235–246.

Oda M., Iwashita K. and Kakiuchi T. (1997) Importance of particle rotation in the mechanics of granular materials, *Powders & Grains*, **97**, 207–210.

Peña A. A., García-Rojo R. and Herrmann H. J. (2007) Influence of particle shape on sheared dense granular media, *Granular Matter*, **9** (3-4), 279-291.

Poeschel T. and Buchholtz V. (1993) Static friction phenomena in granular materials: Coulomb law versus particle geometry, *Phys. Rev. Lett.*, **71** (24), 3963–3966.

Rojek J. (2007) Discrete element modelling of rock cutting, *Computer Methods in Materials Science*, **7** (2), 224–230.

Rothenburg L. and Bathurst R. J. (1992) Micromechanical features of granular materials with planar elliptical particles, *Geotechnique*, **42** (1), 79–95.

Tejchman J. and Wu W. (1993) Numerical study on shear band patterning in a Cosserat continuum, *Acta Mechanica*, **99**, 61–74.

Tejchman J. (2004) Influence of a characteristic length on shear zone formation in hypoplasticity with different enhancements, *Computers and Geotechnics*, **31** (8), 595–611.

Thornton C., Yin K. K. and Adams M. J. (1996) Numerical simulation of the impact fracture and fragmentation of agglomerates, *J. Phys.*, D 29, 424–435.

Wu W. (1992) *Hypoplastizität als mathematisches Modell zum mechanischen Verhalten granularer Stoffe*, Heft 129, Institute for Soil- and Rock-Mechanics, University of Karlsruhe.

Zhu H. P., Zhou Z. Y., Yang R. Y. and Yu A. B. (2007) Discrete particle simulation of particulate systems: Theoretical developments, *Chem. Eng. Sci.*, **62**, 3378–3396.

APPENDIX A

Table 2. Formulae used to calculate interactions between two spheres: displacements, rotations, velocities, forces and moment (all symbols are listed in List of Symbols)

No.	Description	Formula
1.1	Calculation of distance between sphere centers A and B	$\Delta \vec{X} = \vec{X}_A - \vec{X}_B$
1.2	Calculation of penetration depth	$U = R_A + R_B - \left\| \Delta \vec{X} \right\|$
1.3	Calculation of contact normal vector	$\vec{N} = \dfrac{\Delta \vec{X}}{\left\| \Delta \vec{X} \right\|}$
1.4	Calculation of center of overlapping volume of two spheres	$\vec{C} = \vec{X}_A + \left(R_A - \dfrac{U}{2} \right) \vec{N}$
1.5	Initial orientation of contacting spheres	$\dot{A}' = \dot{A}$ $\dot{B}' = \dot{B}$
1.6	Calculation of contact normal stiffness K_n	$K_n = 2 \dfrac{E_c R_A R_B}{R_A + R_B}$
1.7	Calculation of contact tangential stiffness K_s	$K_s = 2 \dfrac{E_c \nu_c R_A R_B}{R_A + R_B}$
1.8	Calculation of contact rotational stiffness K_r	$K_r = \beta K_s R_A R_B$
1.9	Calculation of contact normal force $\vec{F}_n$	$\vec{F}_n = K_n U \vec{N}$
1.10	Calculation of total velocity increment at contact point of two spheres	$\Delta \vec{V} = \left[\left(\vec{V}_B + \vec{\omega}_B \times \left(-R_B \vec{N} \right) \right) + \right.$ $\left. - \left(\vec{V}_A + \vec{\omega}_A \left(R_A \vec{N} \right) \right) \right]$
1.11	Calculation of normal and tangential velocity increment at contact point of two spheres	$\Delta \vec{V}_n = \left(\vec{N} \cdot \Delta \vec{V} \right) \vec{N}, \Delta \vec{V}_s =$ $= \Delta \vec{V} - \left(\vec{N} \cdot \Delta \vec{V} \right) \vec{N}$
1.12	Calculation of tangential displacement increment at contact point of two spheres	$\Delta \vec{X}_s = \Delta \vec{V}_s \Delta t$
1.13	Calculation of total shear force $\vec{F}_s$	$\vec{F}_s = 0,$ if contact began, otherwise $\vec{F}_s = \vec{F}_s + K_s \Delta \vec{X}_s$
1.14	Correction of total tangential force if Coulomb criterion is not satisfied $\left\| \vec{F}_s \right\| - \left\| \vec{F}_n \right\| \tan \mu \geq 0$	$\vec{F}_s = \vec{F}_s \dfrac{\left\| \vec{F}_n \right\| \tan \mu}{\left\| \vec{F}_s \right\|}$
1.15	Calculation of total forces acting on spheres A and B	$\vec{F}_A = \vec{F}_A - \left(\vec{F}_n + \vec{F}_s \right)$ $\vec{F}_B = \vec{F}_B - \left(\vec{F}_n + \vec{F}_s \right)$

Table 2 continued

1.16	Calculation of total moment acting on spheres A and B (due to F_n and F_s)	$\vec{M}_A = \vec{M}_A - \left(\vec{C} - \vec{X}_A\right) \times \left(\vec{F}_n + \vec{F}_s\right)$ $\vec{M}_B = \vec{M}_B - \left(\vec{C} - \vec{X}_B\right) \times \left(\vec{F}_n + \vec{F}_s\right)$
1.17	Calculation of angular orientation displacement increment (a unit quaternion) $\Delta\dot{Q}$ between two spheres (on the basis of original relative orientation and current relative orientation)	$\Delta\dot{Q} = \dot{A}\left(\dot{A}'\right)^{-1} \dot{B}'\left(\dot{B}\right)^{-1}$
1.18	Conversion of quaternion increment $\Delta\dot{Q} = a + bi + cj + dk$ into three-dimensional rotation vector increment $\Delta\vec{\omega} = \{x, y, z\}$ (if rotation angle $\phi = 0$, zeros are assigned to axes x, y and z)	$\Delta\vec{\omega} = \begin{cases} x = \phi \dfrac{b}{\sin(\phi/2)} \\ y = \phi \dfrac{c}{\sin(\phi/2)} \\ z = \phi \dfrac{d}{\sin(\phi/2)} \end{cases}$, $\phi = 2\arccos(a)$
1.19	Calculation of contact moment increment $\Delta\vec{M}$ between two spheres (rotational stiffness for twist and bending has the same value K_r),	$\Delta\vec{M} = K_r \Delta\vec{\omega}$
1.20	Correction of contact moment vector if criterion $\left\|\vec{M}\right\| - \eta \dfrac{R_A + R_B}{2} \left\|\vec{F}_n\right\| \geq 0$ is not satisfied	$\vec{M} = \vec{M} \dfrac{\eta \dfrac{R_A + R_B}{2} \left\|\vec{F}_n\right\|}{\left\|\vec{M}\right\|}$
1.21	Calculation of current moment acting on spheres A and B (due to M)	$\vec{M}_A = \vec{M}_A - \vec{M}$ $\vec{M}_B = \vec{M}_B + \vec{M}$
1.22	Consideration of gravity (g=9.81 m/s^2)	$\vec{F} = \vec{F} + mg$
1.23	Calculation of local non-viscous damping for forces and moment	$\vec{F} = \vec{F} - \alpha \cdot \text{sgn}(\vec{V})\left|\vec{F}\right|$ $\vec{M} = \vec{M} - \alpha \cdot \text{sgn}(\vec{\omega})\left|\vec{M}\right|$
1.24	Calculation of accelerations according to Newton's 2nd law on the basis of forces and moments ($I_i = \frac{2}{5}R_i^2$)	$\vec{a} = \vec{F}/m$ $\dot{\vec{\omega}} = \vec{M}/I$
1.25	Calculation of current velocities and displacements	$\vec{V} = \vec{V} + \vec{a}\Delta t$ $\vec{X} = \vec{X} + \vec{V}\Delta t$
1.26	Calculation of current angular velocities and rotations	$\dot{\vec{\omega}} = \dot{\vec{\omega}} + \ddot{\vec{\omega}}\Delta t$ $\vec{\omega} = \vec{\omega} + \dot{\vec{\omega}}\Delta t$